Supporting Information for

Ternary Strategy Enabling High-Efficiency Rigid and Flexible Organic Solar Cells with Reduced Nonradiative Voltage Loss

Xiaopeng Duan,[a] Wei Song,[b] Jiawei Qiao,[c] Xiaoming Li,[a] Yunhao Cai,[a] Hongbo Wu,[d] Jie Zhang,[e] Xiaotao Hao,[c] Zheng Tang,*[d] Ziyi Ge,*[b] Fei Huang[e] and Yanming Sun*[a]

Experimental Section

Materials

All purchased materials were used without further purification. PM6, BTP-eC9 and 2,2'-((12,13-bis(2-butyldecyl)-3,9-diundecyl-12,13-dihydro-[1,2,5]-thiadiazolo[3,4-*e*]thieno[2",3":4',5']thieno[2',3':4,5]pyrrolo[3,2-*g*]thieno[2',3':4,5]thieno[3,2-*b*]indole-2,10-diyl)bis(methane-lylidene))bis(5,6-dichloro-1*H*-indene-1,3(2*H*)-dione) (ZY-4Cl) were purchased from Solarmer Materials Inc. The number-average molecular weight (M_n) and PDI of PM6 are 41 kDa and 2.39, respectively. PEDOT:PSS (Clevios P VP.Al 4083) was obtained from Heraeus. Chloroform and 1,8-Diiodooctane were purchased from Sigma Aldrich.

Rigid device fabrication

Both the binary and ternary devices were fabricated with a conventional device structure of ITO/PEDOT:PSS/Active layer/PNDIT-F3N/Ag. The ITO glass was cleaned by ultrasonic treatment in acetone, detergent, distilled water and isopropanol for 20 min, respectively. Next, the ITO glass was treated 2 min air plasma after drying in oven overnight. PEDOT:PSS was spin-cast onto the ITO surface at 4000 rpm for 30 s (the thickness is ~40 nm), and thermal annealed at 150 °C for 20 min in air. Then the active layers with different amounts of ZY-4Cl were spin-cast on the PEDOT:PSS surface in a N_2-filled glove box at 2800 rpm for 40 s with the total concentration of 17 mg mL^{-1} in CF. The weight ratio of the donor and acceptor was kept at 1:1.3, and 0.3% DIO was added into the solutions as an solvent additive. Subsequently, the blend films were treated with thermal annealing at 100 °C for 8 min. The mixture of methanol and acetic acid with PNDIT-F3N (1.2 mg mL^{-1}) was spin-cast on the active layer at 4200 rpm. Finally, 100 nm Ag layer was thermally deposited as the top electrode under high vacuum (~3×10^{-4} Pa) and the device was completed. The active area of the device is 5.12 mm^2, and the mask area is 3.153 mm^2.

Flexible device fabrication

The flexible device was fabricated with a traditional sandwich structure: Ag NWs/PEDOT:PSS/active layer/PFNDI-Br/Ag. The flexible electrode was fabricated through a facile spin-coating Ag NWs solution of 2 mg mL^{-1} at a speed of 4,000 rpm, followed by annealing at 100 °C for 30 min. Then, PEDOT:PSS consisting of 5 wt % xylitol and 0.5 vol % PEG-TmDD was spin coated at a speed of 4,000 rpm on the Ag NWs/substrates followed by thermal annealing at 80 °C for 10 min. Except for

replacing PNDIT-F3N with PFNDI-Br, the subsequent process conditions were the same as those of the rigid device. The area of single flexible cell was 4.0 mm^2.

Measurements and Characterizations

UV-vis absorption spectra were measured using a UV-vis spectrophotometer (Shimadzu UV-3600). The solar-cell performance test used an Air Mass 1.5 Global (AM 1.5 G) solar simulator (SS-F5-3A, Enlitech) with an irradiation intensity of 100 mW cm^{-2}, which was measured by a calibrated silicon solar cell (SRC2020, Enlitech). The *J–V* curves were measured using a Keithley 2400 Source Measure Unit. EQE spectra were measured by using a solar-cell spectral-response measurement system (QE-R3011, Enlitech). Electrical impedance spectroscopy (EIS) of the OSCs was performed in a frequency range from 1 MHz to 10 mHz using Zahner electrochemical workstation at an applied bias equivalent to the open-circuit voltage of the cell under 1 sun illumination. The hole mobility and electron mobility of the blend films were measured under dark by the space charge limited current (SCLC) method with hole-only device structure of ITO/PEDOT:PSS/active layer/MoO_3/Ag and electron-only device structure of ITO/ZnO/active layer/PNDIT-F3N/Ag. The mobilities (μ) were determined by fitting the dark current to the model of a single carrier SCLC, described by the equation: $J = (9/8)\varepsilon_r\varepsilon_0\mu(V^2/L^3)$, where J is the current density, ε_r is the dielectric permittivity of the active layer, ε_0 is the vacuum permittivity, L is the thickness of the active layer and V is the effective voltage. The effective voltage can be obtained by subtracting the built-in voltage (V_{bi}) and the voltage drop (V_s) from the substrate's series resistance from the applied voltage (V_{appl}), $V=V_{appl}-V_{bi}-V_s$. The mobility can be calculated from the slope of the $J^{0.5}\sim V$ curves. Steady state photoluminescence (PL) was collected by a spectrometer (DU420A-OE, ANDOR). Fluorescence decay dynamics were tracked by TCSPC (Becker&Hickl, SPC-150). The excitation wavelength was 400 nm. The excitation power of all the PL spectra and TRPL experiments were fixed at 4 μW. Considering the repetition rate of the laser with 80 MHz, each pulse has the energy of $E= 5\times10^{-14}$ J. The diameter of the laser spot was about 8 μm and its area was calculated as $S= 5.02\times10^{-7}$ cm^2. Atomic force microscopy (AFM) images were performed on a Dimension Icon AFM (Bruker) in a tapping mode. The Two-dimensional grazing incidence X-ray diffraction (2D-GIXRD) measurement was performed by detector Pilatus3R 1M, Dectris (X-ray Source: MetalJet-D2, Excillum). Femtosecond transient absorption spectroscopy measurements were performed on an Ultrafast Helios pump-probe system in collaboration with a regenerative amplified

laser system from Coherent. An 800 nm pulse with a repetition rate of 1 kHz, a length of 100 fs, and pump fluence of 0.7 μJ cm^{-2}, was generated by a Ti: sapphire amplifier (Astrella, Coherent). Then the 800 nm pulse was separated into two parts by a beam splitter. One part was coupled into an optical parametric amplifier (TOPAS, Coherent) to generate the pump pulses at 400 nm. The other part was focused onto a sapphire plate and a YAG plate to generate white light supercontinuum as the probe beams with spectra covering 420~800 nm and 750~1600 nm, respectively. The time delay between pump and probe was controlled by a motorized optical delay line with a maximum delay time of 8 ns. The samples films were spin-coated onto the 1 mm-thick quartz plates and are encapsulated by epoxy resin in nitrogen-filled glove box to resist water and oxygen in the air. The pump pulse is chopped by a mechanical chopper with 500 Hz and then focused on to the mounted sample with probe beams. The probe beam was collimated and focused into a fiber-coupled multichannel spectrometer with CCD sensor. The energy of pump pulse was measured and calibrated by a power meter (PM400, Thorlabs). The EL spectra were measured using a Shamrock SR-303i spectrometer from Andor Tech with a Newton EM-CCD Si and an iDus InGaAs array detector at -60 °C. EQE_{EL} measurements were done using a home-built setup using a Keithley 2400 to inject current to the solar cells. Emission photon-flux from the solar cells was recorded using a Si detector (Hamamatsu s1337-1010BQ) and a Keithley 6482 picoammeter. Sensitive EQE measurements were done using a halogen lamp light source, chopped at a frequency of 173 Hz, a monochromator (Newport CS260), a Stanford SR830 lock-in amplifier, a Stanford SR570 current amplifier, and a set of long pass filters.

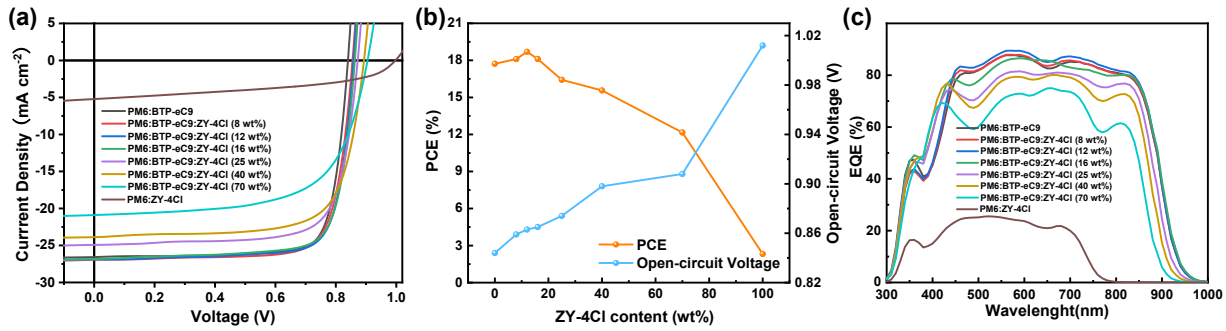

Figure S1. a) Current–voltage (*J-V*) characteristics of the ternary devices with different amounts of ZY-4Cl under simulated AM 1.5 G illumination at 100 mW cm^{-2}. b) The dependence curves of PCE and open circuit voltage (V_{oc}) of the ternary devices on the ZY-4Cl content, and c) the corresponding EQE curves.

Table S1. Summary of photovoltaic parameters of the ternary devices with different ZY-4Cl contents.

Active layer	V_{oc} (V)	J_{sc} (mA cm^{-2})	FF(%)	PCE[a)](%)
PM6:BTP-eC9	0.844 (0.842±0.003)	26.84 (26.61±0.21)	78.2 (77.7±0.3)	17.72 (17.43±0.14)
PM6:BTP-eC9:ZY-4Cl (8 wt%)	0.859 (0.857±0.002)	26.91 (26.73±0.28)	78.3 (78.0±0.2)	18.10 (17.79±0.17)
PM6:BTP-eC9:ZY-4Cl (12 wt%)	0.863 (0.862±0.002)	27.40 (27.14±0.25)	79.0 (78.8±0.4)	18.69 (18.33±0.15)
PM6:BTP-eC9:ZY-4Cl (16 wt%)	0.865 (0.863±0.002)	26.84 (26.60±0.25)	78.0 (77.8±0.3)	18.11 (17.75±0.18)
PM6:BTP-eC9:ZY-4Cl (25 wt%)	0.874 (0.872±0.002)	24.95 (24.67±0.29)	75.3 (75.1±0.3)	16.42 (16.03±0.16)
PM6:BTP-eC9:ZY-4Cl (40 wt%)	0.898 (0.896±0.002)	23.89 (23.69±0.22)	72.5 (72.3±0.2)	15.56 (15.22±0.16)
PM6:BTP-eC9:ZY-4Cl (70 wt%)	0.908 (0.906±0.002)	20.90 (20.68±0.22)	64.1 (63.9±0.1)	12.16 (11.85±0.15)
PM6:ZY-4Cl	1.012 (1.010±0.003)	5.12 (4.62±0.28)	45.4 (43.3±1.4)	2.32 (1.98±0.14)

[a)]Average values with standard deviation were obtained from 30 devices.

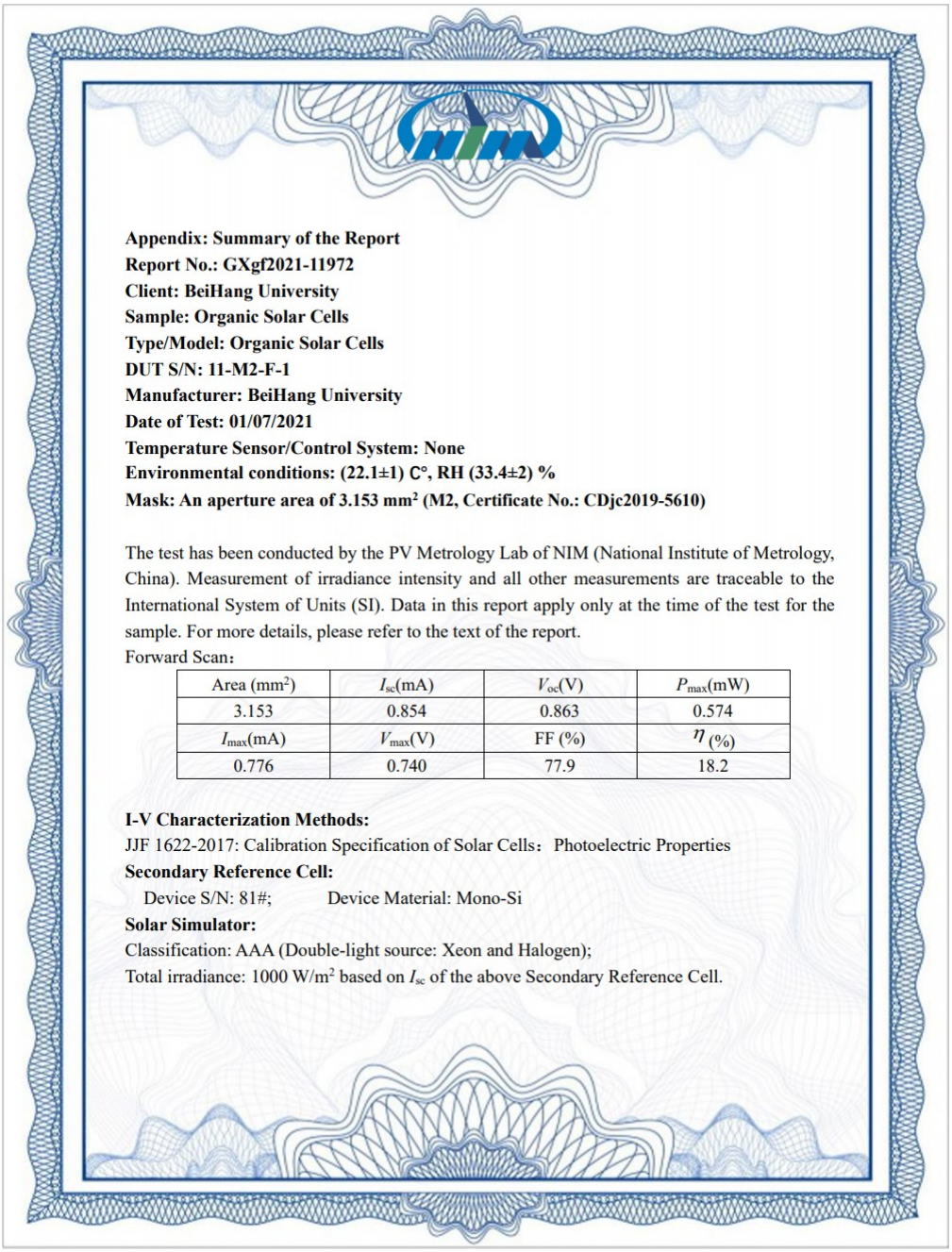

Appendix: Summary of the Report
Report No.: GXgf2021-11972
Client: BeiHang University
Sample: Organic Solar Cells
Type/Model: Organic Solar Cells
DUT S/N: 11-M2-F-1
Manufacturer: BeiHang University
Date of Test: 01/07/2021
Temperature Sensor/Control System: None
Environmental conditions: (22.1±1) C°, RH (33.4±2) %
Mask: An aperture area of 3.153 mm² (M2, Certificate No.: CDjc2019-5610)

The test has been conducted by the PV Metrology Lab of NIM (National Institute of Metrology, China). Measurement of irradiance intensity and all other measurements are traceable to the International System of Units (SI). Data in this report apply only at the time of the test for the sample. For more details, please refer to the text of the report.

Forward Scan:

Area (mm^2)	I_{sc}(mA)	V_{oc}(V)	P_{max}(mW)
3.153	0.854	0.863	0.574
I_{max}(mA)	V_{max}(V)	FF (%)	η (%)
0.776	0.740	77.9	18.2

I-V Characterization Methods:
JJF 1622-2017: Calibration Specification of Solar Cells：Photoelectric Properties
Secondary Reference Cell:
Device S/N: 81#; Device Material: Mono-Si
Solar Simulator:
Classification: AAA (Double-light source: Xeon and Halogen);
Total irradiance: 1000 W/m² based on I_{sc} of the above Secondary Reference Cell.

Figure S2. The certification report for the PM6:BTP-eC9:ZY-4Cl device from National Institute of Metrology (NIM), China.

Table S2. Summary of the recent progress of OSCs with verified PCEs of over 17%.

Active layer	V_{oc} (V)	J_{sc} (mA cm^{-2})	FF (%)	PCE (%)	Certified PCE (%)	Ref.
PM6:Y6	0.840	26.09	79.1	17.32	17.10	1
PM1:Y6	0.870	25.90	78.0	17.60	17.03	2
PM6:BTP-eC9	0.839	26.20	81.1	17.80	17.25	3
PM6:PM7:Y6:$PC_{71}BM$	0.859	26.55	79.2	18.07	17.35	4
PM6:Y6:Y6-BO:PCBM	0.852	26.67	78.5	17.84	17.42	5
D18-Cl:N3	0.859	27.85	75.7	18.13	17.56	6
D18:Y6	0.859	27.70	76.6	18.22	17.61	7
PM6:BTP-eC9	0.852	27.60	78.3	18.41	17.90	8
PM6:BTP-4Cl-BO:BTP-T-3Cl	0.857	27.38	77.7	18.21	17.91	9
PM6:L8-BO	0.870	25.72	81.5	18.32	17.91	10
PM6:BTP-eC9:BTP-F	0.858	26.99	79.7	18.45	18.02	11
PM6:BO-4Cl:Y6-1O	0.855	27.46	79.0	18.52	18.10	12
PM6:BTP-eC9:L8-BO-F	0.853	27.35	80.0	18.66	18.15	13
PB2F:PBDB-TF:BTP-eC9	0.863	26.80	80.4	18.60	18.18	14
PM6:L8-BO	0.893	26.03	80.0	18.60	18.20	15
D18-Cl-B:N3:$PC_{61}BM$	0.836	28.50	78.7	18.74	18.21	16
PM6:BTP-eC9:ZY-4Cl	**0.863**	**27.40**	**79.0**	**18.69**	**18.21**	**Our work**
PBDB-TF:HDO-4Cl:BTP-eC9	0.866	27.05	80.5	18.86	18.33	17

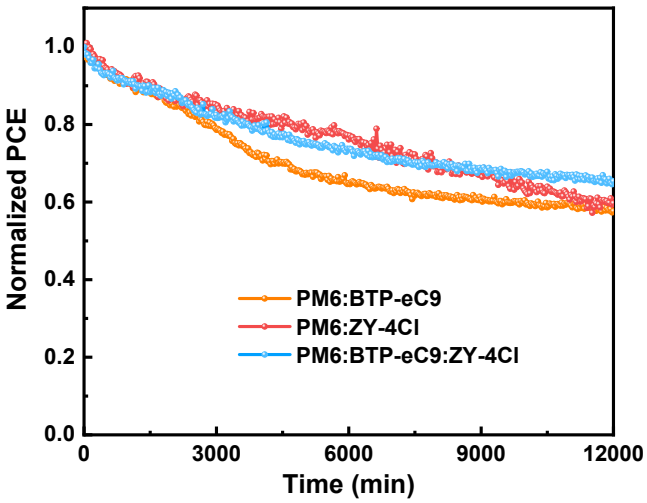

Figure S3. Long-term stability of the solar cells under continuous illumination at 100 mW/cm^2 in air.

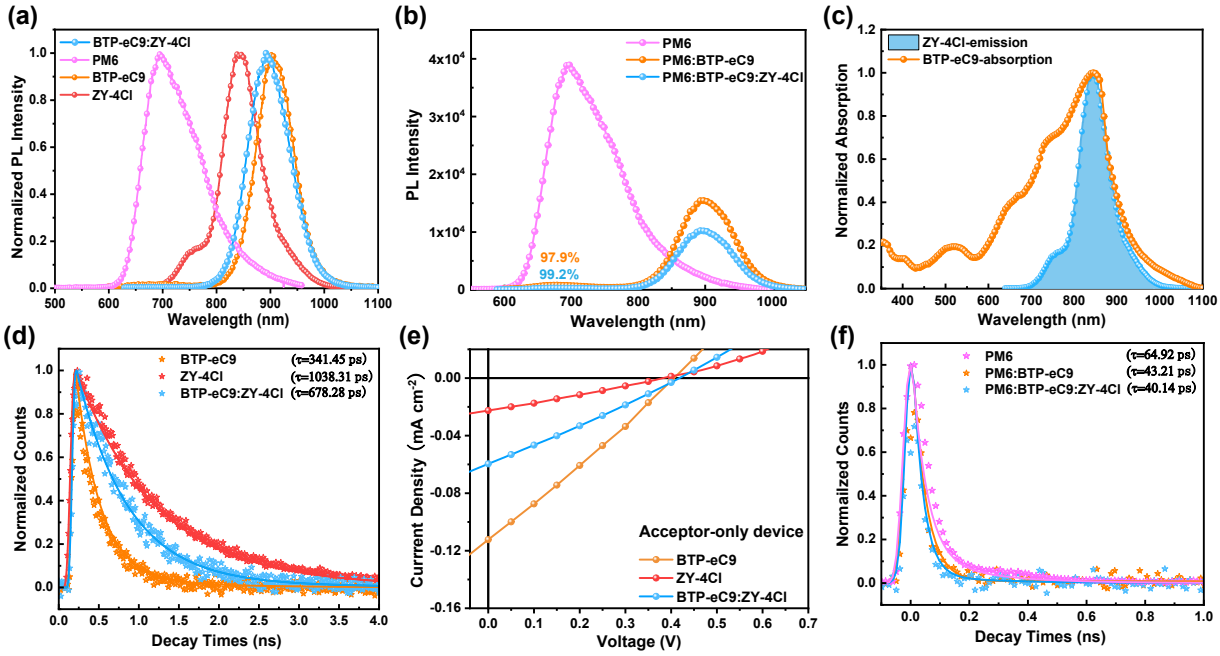

Figure S4 a) Normalized PL spectra of PM6, BTP-eC9, ZY-4Cl and BTP-eC9:ZY-4Cl. b) PL spectra of PM6, PM6:BTP-eC9 and PM6:BTP-eC9:ZY-4Cl. c) PL spectrum of ZY-4Cl and UV absorption spectrum of BTP-eC9. d) TRPL spectra of BTP-eC9, ZY-4Cl and BTP-eC9:ZY-4Cl. e) *J-V* characteristics of OSCs based on BTP-eC9, ZY-4Cl and BTP-eC9:ZY-4Cl. f) TRPL spectra of PM6, PM6:BTP-eC9 and PM6:BTP-eC9:ZY-4Cl.

Table S3. Summary of photovoltaic parameters of the acceptor-only devices.

Samples	V_{oc}	J_{sc}	FF	PCE
BTP-eC9	0.406	0.112	26.6	0.012
ZY-4Cl	0.383	0.023	26.8	0.002
BTP-eC9:ZY-4Cl	0.418	0.060	26.6	0.007

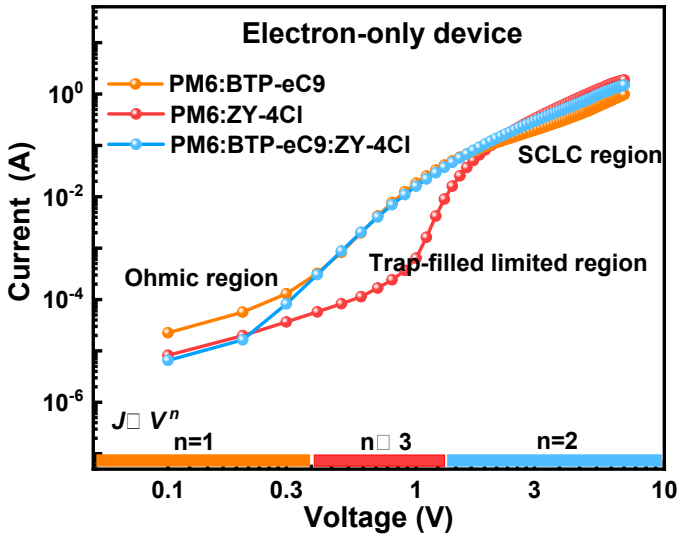

Figure S5 *J-V* characteristics of electron-only devices of binary and ternary blends.

Table S4. The mobilities and corresponding defect densities (n_t) of the binary and ternary devices.

Samples	Hole mobility μ_h ($cm^2\ V^{-1}\ s^{-1}$)	Electron mobility μ_e ($cm^2\ V^{-1}\ s^{-1}$)	μ_h/μ_e	V_{TFL} (V)	n_t (cm^{-3})
PM6:BTP-eC9	3.70×10^{-4}	2.99×10^{-4}	1.24	0.437	1.136×10^{16}
PM6:ZY-4Cl	2.21×10^{-4}	1.27×10^{-4}	1.74	0.841	1.923×10^{16}
PM6:BTP-eC9:ZY-4Cl	3.84×10^{-4}	3.23×10^{-4}	1.19	0.434	1.089×10^{16}

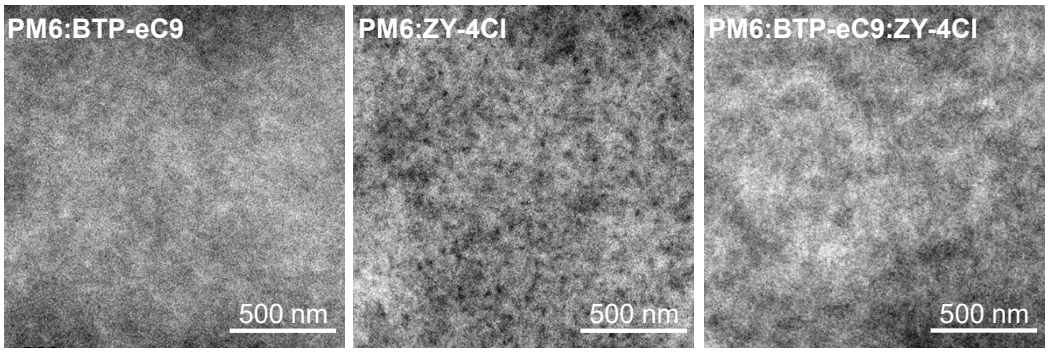

Figure S6. TEM phase images of the binary and ternary blend films.

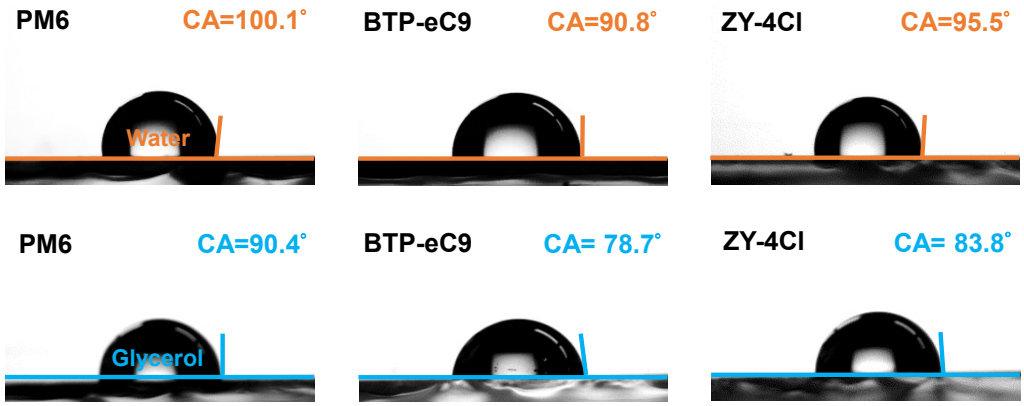

Figure S7. Contact angles of the single-component films.

Table S5. Contact angle and surface tension data of the single-component films.

Surface	θ_{Water} (°)	θ_{EG} (°)	γ (mN m^{-1})
PM6	100.1	90.4	20.9
BTP-eC9	90.8	78.7	27.1
ZY-4Cl	95.5	83.8	24.4

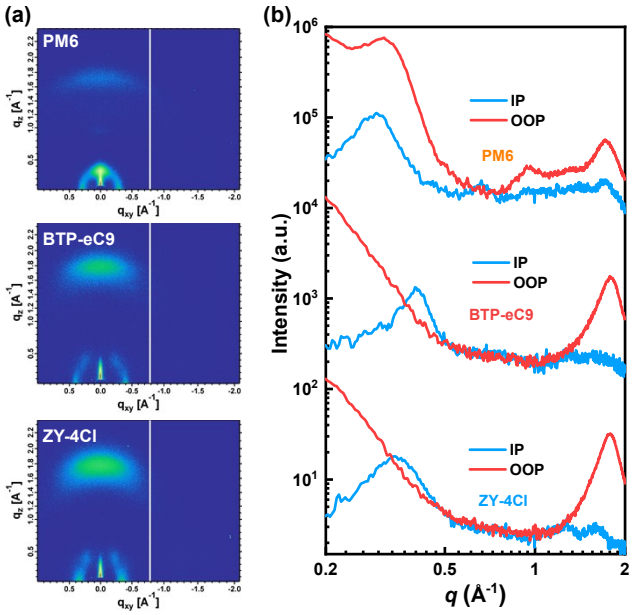

Figure S8. a) 2D GIWAXS pattern and b) IP and OOP line-cut profiles of the PM6, BTP-eC9 and ZY-4Cl films.

Table S6. Crystal Coherence lengths and the *d*-spacing for the neat films.

Samples	In plane				Out of plane			
	Location (Å^{-1})	*d*-spacing[a)] (Å)	FWHM	CCL[b)] (Å)	Location (Å^{-1})	*d*-spacing[a)] (Å)	FWHM	CCL[b)] (Å)
PM6	0.292	21.55	0.088	63.69	1.718	3.66	0.331	16.89
BTP-eC9	0.396	15.87	0.116	48.08	1.780	3.53	0.309	18.10
ZY-4Cl	0.343	18.32	0.153	36.60	1.773	3.54	0.302	18.51

[a)] Obtained by the equation of $d = 2\pi/q$, in which q corresponds to the diffraction peak positions;

[b)] Calculated using the equation: CCL = 2 $\pi K/w$, in which w is the full width at half maxima and K is a form factor (0.89 here).

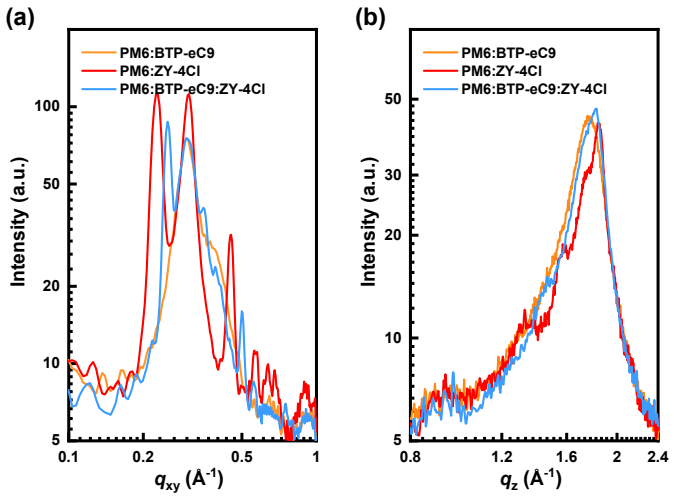

Figure S9. (a) In-plane and (b) out-of-plane line-cuts of the binary and ternary blends.

Table S7. Crystal Coherence lengths and the *d*-spacing for the binary and ternary blends.

Samples	In plane				Out of plane			
	Location (Å^{-1})	*d*-spacing[a)] (Å)	FWHM	CCL[b)] (Å)	Location (Å^{-1})	*d*-spacing[a)] (Å)	FWHM	CCL[b)] (Å)
PM6:BTP-eC9	0.298	21.05	0.043	118.47	1.770	3.55	0.270	20.74
PM6:ZY-4Cl	0.227	27.68	0.024	235.08	1.839	3.42	0.211	26.50
	0.303	20.74	0.043	130.05				
	0.450	13.96	0.023	243.13				
PM6:BTP-eC9:ZY-4Cl	0.250	25.13	0.018	310.67	1.823	3.45	0.251	22.28
	0.300	20.94	0.051	109.65				
	0.502	12.52	0.023	247.11				

[a)] Obtained by the equation of $d = 2\pi/q$, in which q corresponds to the diffraction peak positions;

[b)] Calculated using the equation: CCL = 2 $\pi K/w$, in which w is the full width at half maxima and K is a form factor (0.89 here).

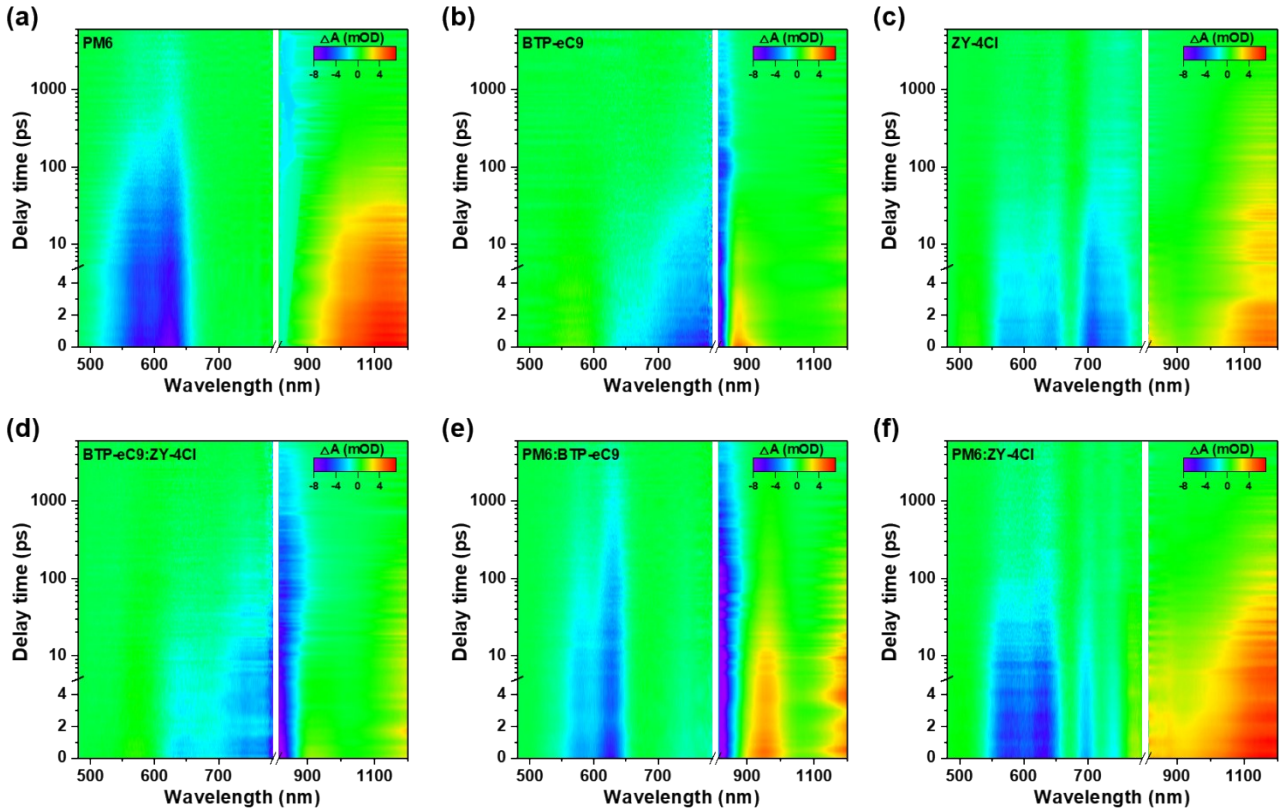

Figure S10. 2D TAS images of the neat and blend films with 400 nm excitation.

Table S8. Fitted parameters for TA kinetics at PM6 GSB of the binary and ternary blends.

Pump @ 400 mn	τ_1 (ps)	A_1	τ_2 (ps)	A_2	τ_3 (ps)	A_3	τ_{ave} (ps)
PM6:ZY-4Cl	0.22	27.2	10.86	58.5	337.03	14.3	54.61
PM6:BTP-eC9	2.37	54.3	36.87	22.5	1996.92	23.2	472.87
PM6:BTP-eC9:ZY-4Cl	2.17	52.8	34.10	28.8	2351.87	18.4	443.71

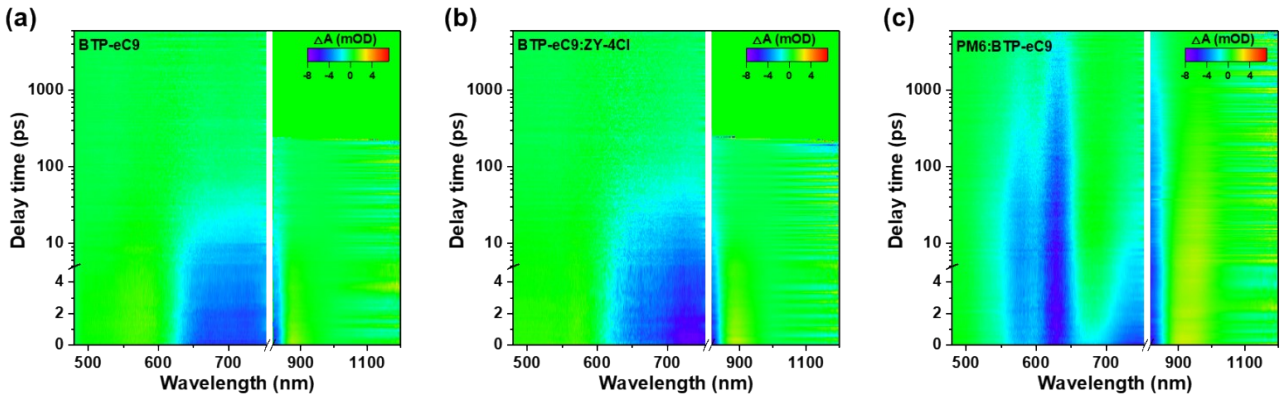

Figure S11. 2D TAS images of the neat and blend films with 800 nm excitation. There were not enough phosphorescence signals detected in the PM6, ZY-4Cl and PM6:ZY-4Cl samples.

Table S9. Fitted parameters for TA kinetics at BTP-eC9 GSB of the binary and ternary blends.

Pump @ 800 mn	**τ_1 (ps)**	**A_1**	**τ_2 (ps)**	**A_2**	**τ_3 (ps)**	**A_3**	**τ_{ave} (ps)**
PM6:BTP-eC9	0.94	10.2	9.94	42.6	1043.65	47.2	496.93
PM6:BTP-eC9:ZY-4Cl	0.13	55.4	6.98	33.3	1294.20	11.3	148.64

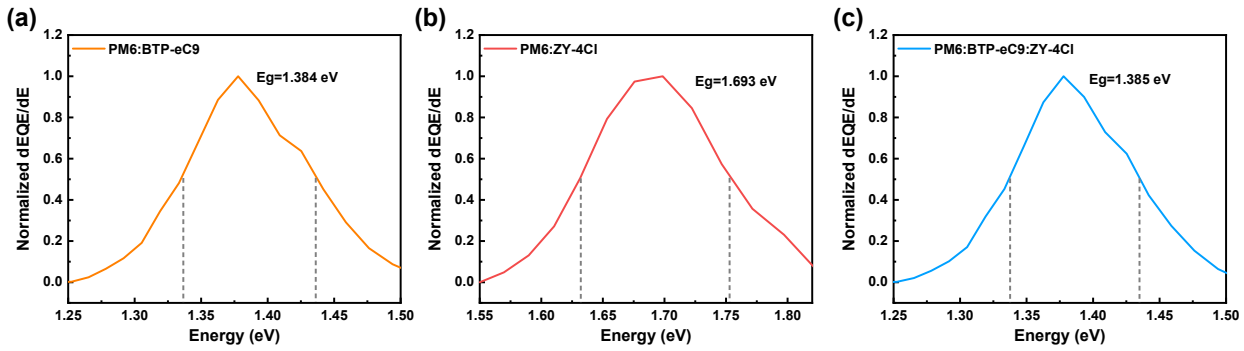

Figure S12. Determination of the E_g of the binary and ternary devices via the derivatives of the EQE spectra. The region between dashed lines is the part where the gap distribution probability is greater than half of the maximum, which is used for the optical gap calculation.[18]

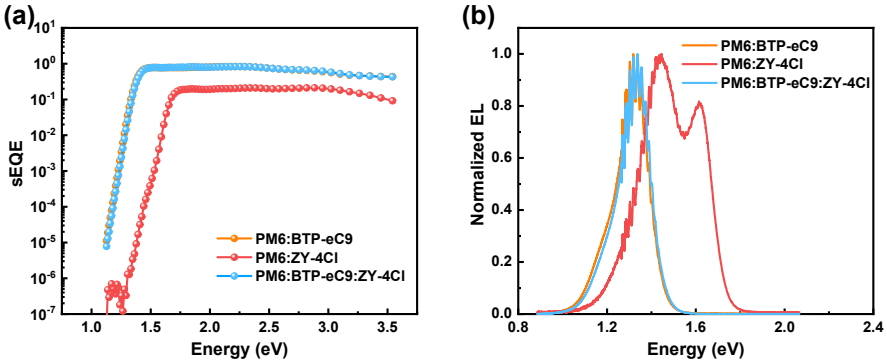

Figure S13. a) Highly sensitive EQE curves. b) Normalized EL curves.

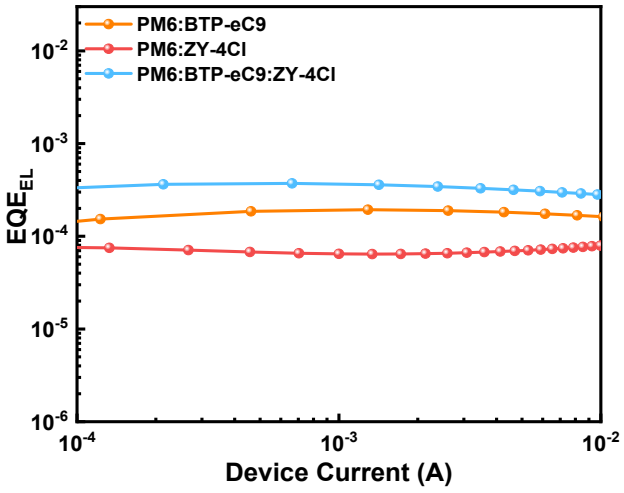

Figure S14. EQE_{EL} spectra of the binary and ternary blends.

References

[1] L. Liu, Y. Kan, K. Gao, J. Wang, M. Zhao, H. Chen, C. Zhao, T. Jiu, A.-K.-Y. Jen, Y. Li, *Adv. Mater.* 2020, **32**, 1907604.

[2] J. Wu, G. Li, J. Fang, X. Guo, L. Zhu, B. Guo, Y. Wang, G. Zhang, L. Arunagiri, F. Liu, H. Yan, M. Zhang, Y. Li, *Nat. Commun.* 2020, **11**, 4612.

[3] Y. Cui, H. Yao, J. Zhang, K. Xian, T. Zhang, L. Hong,Y. Wang, Y. Xu, K. Ma, C. An, C. He, Z. Wei, F. Gao, J. Hou, *Adv. Mater.* 2020, **32**, 1908205.

[4] M. Zhang, L. Zhu, G. Zhou, T. Hao, C. Qiu, Z. Zhao, Q. Hu, B. W. Larson, H. Zhu, Z. Ma, Z. Tang, W. Feng, Y. Zhang, T. P. Russell, F. Liu, *Nat. Commun.* 2021, **12**, 309.

[5] M. Zhang, L. Zhu, T. Hao, G. Zhou, C. Qiu, Z. Zhao, N. Hartmann, B. Xiao, Y. Zou, W. Feng, H. Zhu, M. Zhang, Y. Zhang, Y. Li, T. P. Russell, F. Liu, *Adv. Mater.* 2021, **33**, 2007177.

[6] J. Qin, L. Zhang, C. Zuo, Z. Xiao, Y. Yuan, S. Yang, F. Hao, M. Cheng, K. Sun, Q. Bao, Z. Bin, Z. Jin, L. Ding, *J. Semicond.* 2021, **42**, 010501.

[7] K. Jin, Z. Xiao, L. Ding, *J. Semicond.* 2021, **42**, 010502.

[8] Y. Qin, Y. Chang, X. Zhu, X. Gu, L.Guo, Y. Zhang, Q. Wang, Ji. Zhang, X. Zhang, X. Liu, K. Lu, E. Zhou, Z. Wei, X. Sun, *Nano Today* 2021, **41**, 101289.

[9] Y. Pan, X. Zheng, J. Guo, Z. Chen, S. Li, C. He, S. Ye, X. Xia, S. Wang, X. Lu, H. Zhu, J. Min, L. Zuo, M. Shi, H. Chen, *Adv. Funct. Mater.* 2021, 2108614. DOI: 10.1002/adfm.202108614.

[10] C. Li, J. Zhou, J. Song, J. Xu, H. Zhang, X. Zhang, J. Guo, L. Zhu, D. Wei, G. Han, J. Min, Y. Zhan, Z. Xie, Y. Yi, H. Yan, F. Gao, F. Liu, Y. Sun, *Nat. Energy* 2021, **6**, 605-613.

[11] Y. Li, Y. Cai, Y. Xie, J. Song, H. Wu, Z. Tang, J. Zhang, F. Huang, Y. Sun, *Energy Environ. Sci.* 2021, 2021, **14**, 5009–5016.

[12] D. Wang, G. Zhou, Y. Li, K. Yan, L. Zhan, H. Zhu, X. Lu, H. Chen, C. Li, *Adv. Funct. Mater.* 2021, **32**, 2107827.

[13] Y. Cai, Y. Li, R. Wang, H. Wu, Z. Chen, J. Zhang, Z. Ma, X. Hao, Y. Zhao, C. Zhang, F. Huang, Y. Sun, *Adv. Mater.* 2021, **33**, 2101733.

[14] T. Zhang, C. An, P. Bi, Q. Lv, J. Qin, L. Hong, Y. Cui, S. Zhang, J. Hou, *Adv. Energy Mater.* 2021, **11**, 2101705.

[15] J. Song, L. Zhu, C. Li, J. Xu, H. Wu, X. Zhang, Y. Zhang, Z. Tang, F. Liu, Y. Sun, *Matter*, 2021, **4**, 2542-2552.

[16] X. Meng, K. Jin, Z. Xiao, L. Ding, *J. Semicond.* 2021, **42**, 100501.

[17] P. Bi, S. Zhang, Z. Chen, Y. Xu, Y. Cui, T. Zhang, J. Ren, J. Qin, L. Hong, X. Hao, J. Hou, *Joule* 2021, **5**, 1–12.

[18] Y. Wang, D. Qian, Y. Cui, H. Zhang, J. Hou, K. Vandewal, T. Kirchartz, F. Gao, *Adv. Energy Mater.* 2018, **8**, 1801352.